

Article

Ce Doping Effects on the Hydrogen Sensing Properties of Graphene/SnO₂-Based Sensors

Zijie Jiao ¹, Lingyun Wang ¹, Xiaotong Xu ¹, Jie Xiang ^{1,2}, Shuiming Huang ^{1,2}, Tao Lu ² and Xueling Hou ^{1,*} 

¹ School of Materials Science and Engineering, Shanghai University, Shanghai 200072, China; jiao_zj@163.com (Z.J.); wly18395354697@163.com (L.W.); xuxiaotong0908@163.com (X.X.); xj@kingmt.com.cn (J.X.); hshuiming@kingmt.com.cn (S.H.)

² Shanghai King Material Technology Ltd., East Huiwang Road, Jiading, Shanghai 201815, China; jw@kingmt.com.cn

* Correspondence: flybird1656@163.com

Abstract: The development of a sensor capable of selectively detecting hydrogen levels in the environment holds immense importance for ensuring the safer utilization of hydrogen energy. In this study, a hydrogen sensor made of Ce-doped single-layer graphene (SLG)/SnO₂ composite material was fabricated using a hydrothermal method. The study examined the impact of varying Ce doping concentrations on the hydrogen sensing capabilities of the SLG/SnO₂ matrix. The results show that the SLG/SnO₂ hydrogen sensor doped with 2 mol% Ce demonstrated optimal performance at a humidity of 20%. It operated most efficiently at 250 °C, with a response of 2.49, representing a 25.75% improvement over the undoped sample. The response/recovery times were 0.46/3.92 s, which are 54.9% shorter than those of the undoped sample. The enhancement in hydrogen sensitivity stems from the synergistic effect of Ce and SLG, which facilitates the coexistence of n–n and p–n heterojunctions, thereby increasing carrier mobility and refining grain structure. Analysis via X-ray photoelectron spectroscopy (XPS) reveals that Ce increases the material's oxygen vacancy concentration, enhancing its hydrogen sensitivity. Ce-doped SLG/SnO₂, with its robust hydrogen sensitivity, represents one of the leading candidates for future hydrogen gas sensors.

Keywords: hydrogen gas sensors; Ce-SnO₂/SLG; doping; Ce; n–n heterojunction; p–n heterojunction



Citation: Jiao, Z.; Wang, L.; Xu, X.; Xiang, J.; Huang, S.; Lu, T.; Hou, X. Ce Doping Effects on the Hydrogen Sensing Properties of Graphene/SnO₂-Based Sensors. *Materials* **2024**, *17*, 4382. <https://doi.org/10.3390/ma17174382>

Academic Editor: Albena Paskaleva

Received: 25 July 2024

Revised: 30 August 2024

Accepted: 2 September 2024

Published: 5 September 2024



Copyright: © 2024 by the authors. Licensee MDPI, Basel, Switzerland. This article is an open access article distributed under the terms and conditions of the Creative Commons Attribution (CC BY) license (<https://creativecommons.org/licenses/by/4.0/>).

1. Introduction

In recent years, people have been advocating and committed to the development and utilization of green and renewable energy, and then applying it to various aspects of people's lives [1]. Compared to other clean energy sources such as solar and wind energy that are limited by the application environment, hydrogen energy has excellent performance such as high combustion efficiency, long-term storage capacity, and low pollution, which enables the more efficient storage and transportation of hydrogen energy, more convenient use, and stable energy supply [2,3]. At present, hydrogen energy is widely used in various fields such as civil, industrial, transportation, power, and energy storage, as well as high-end fields such as aviation [4]. However, pure H₂ is colorless, odorless, tasteless, and suffocating, making it difficult for humans to detect leaks when they occur [5]. And hydrogen has an explosion limit of 4–75%, meaning that any hydrogen leak has a high risk of causing an explosion. Therefore, developing a sensor that can selectively detect hydrogen content in the environment is of great significance for the safer application of hydrogen energy [6]. Metal oxide semiconductors (MOs), such as TiO₂, ZnO, WO₃, In₂O₃, SnO₂, etc., have been widely studied as core hydrogen sensitive materials for hydrogen sensors [7–12]. SnO₂ is a typical N-type semiconductor with a bandgap width of 3.6 eV. SnO₂-based hydrogen sensors have attracted much attention due to their low cost, excellent chemical durability, and simple preparation process [13–15]. In addition, the abundant oxygen vacancies in SnO₂ nanomaterials give them excellent conductivity properties [2].

Based on these characteristics, SnO₂ nanomaterials have been widely used in gas sensors. There are many methods to prepare SnO₂ nanomaterial hydrogen sensors, mainly including magnetron sputtering, atomic deposition, sol-gel, and hydrothermal methods. Among them, the hydrothermal method has high purity and a uniform particle size, which is suitable for preparing SnO₂ nanomaterial hydrogen sensors.

However, pure SnO₂ nanomaterials have problems such as a long response/recovery time, high operating temperature, and poor selectivity [16,17]. Therefore, in recent years, a large number of scholars have adopted various methods to improve these problems, such as material microstructure design, precious metal composites, heterojunction generation, and doping modification [18–22]. Scholars have modified it by adding graphene. The unique 2D structure of graphene makes it highly sensitive to its surrounding environment, and its surface adsorption properties can enable the application of sensor materials [23]. Ch. Seshendra Reddy et al. [24] found that electrospun derived Al-doped SnO₂ embedded by graphene nanotubes has a high response and low response/recovery time. Li et al. [25] used a Au_xSn intermetallic compound, modifying the reduced graphene oxide (rGO) modified SnO₂ (Au_xSn-rGO-SnO₂) to detect H₂. They found that Au_xSn-rGO-SnO₂ nanocomposites showed a rapid and high response to H₂. In addition, many studies have shown that doping modification is an effective method to improve the response, selectivity, optimal operating temperature, and response/recovery time of SnO₂-based sensors. Doping is a technique of introducing impurity elements during material synthesis and preparation, which can change the morphology of materials or introduce catalysts to promote reactions, thereby improving the response of sensors and enhancing their performance [26–28]. This doping method can change the crystal structure of the material, introduce impurity energy levels, and increase oxygen vacancies, thereby accelerating the response and adsorption (desorption) rate of the sensor, and optimizing the sensing characteristics [2,26,29–31]. Singh et al. [32] found that SnO₂ sensors doped with 3% Er exhibited stronger sensor response and temperature-dependent selectivity toward ethanol and hydrogen. David E. Motaung et al. [33] reported that a CeO₂-SnO₂ mixed oxide heterostructure exhibits a good response to H₂ gas, high sensitivity, good repeatability, and selectivity. They believe that the n–n heterojunction formed between CeO₂ and SnO₂ is the main reason for its improved performance.

According to previous research, the composite material formed by adding 4 mg SLG and SnO₂ has the best performance [34]. Therefore, this article studied the effect of doping different amounts of Ce in SnO₂/SLG-4 mg substrate material on hydrogen sensing performance. It was found that the hydrogen sensitivity of the material was optimal when the doping amount of Ce was 2 mol%. The main reason for the enhanced hydrogen sensitivity performance is the coexistence of a n–n heterojunction and n–p heterojunction in doped materials, which increases the carrier migration rate, grain refinement, oxygen vacancy concentration, and the increase in active sites caused by graphene.

2. Materials and Methods

2.1. Synthesis of S-4G

SnO₂/SLG were prepared using a hydrothermal method. The detailed preparation process is shown in Figure 1. Firstly, 1.02 mmol of SnCl₂·2H₂O, 4 mg of SLG, and 12.45 mmol of H₂NCONH₂ powder were weighed. The weighed powder was mixed and poured into 60 mL of anhydrous ethanol, sonicated for 10 min, and then stirred with a magnetic stirrer for 30 min. The stirred solution was transferred to a reaction vessel and reacted at 16 °C for 12 h. The final product was collected by centrifugation and washed with anhydrous ethanol six times. Afterward, the completely dry white powder was placed at 500 °C for 2 h to obtain SnO₂/SLG samples, labeled S-4G.

2.2. Synthesis of S-4G-xC

$x\text{Ce-SnO}_2/\text{SLG}$ ($x = 1, 2, 3$ mol%) were prepared using the hydrothermal method. The detailed preparation process is shown in Figure 1. Firstly, 1.02 mmol of $\text{SnCl}_2 \cdot 2\text{H}_2\text{O}$, x mol% of $\text{CeCl}_2 \cdot 6\text{H}_2\text{O}$ ($x = 1, 2, 3$), 4 mg of SLG, and 12.45 mmol of H_2NCONH_2 powder were weighed. The weighed powder was mixed and poured into 60 mL of anhydrous ethanol, sonicated for 10 min, and then stirred with a magnetic stirrer for 30 min. The stirred solution was transferred to a reaction vessel and reacted at 160°C for 12 h. The stirred solution was transferred to a reaction vessel and reacted at 160°C for 12 h. The final product was collected by centrifugation and washed with anhydrous ethanol six times. Afterward, the completely dry white powder was placed at 500°C for 2 h to obtain $x\text{Ce-SnO}_2/\text{SLG}$ ($x = 1, 2, 3$) samples, labeled S-4G-xC ($x = 1, 2, 3$).

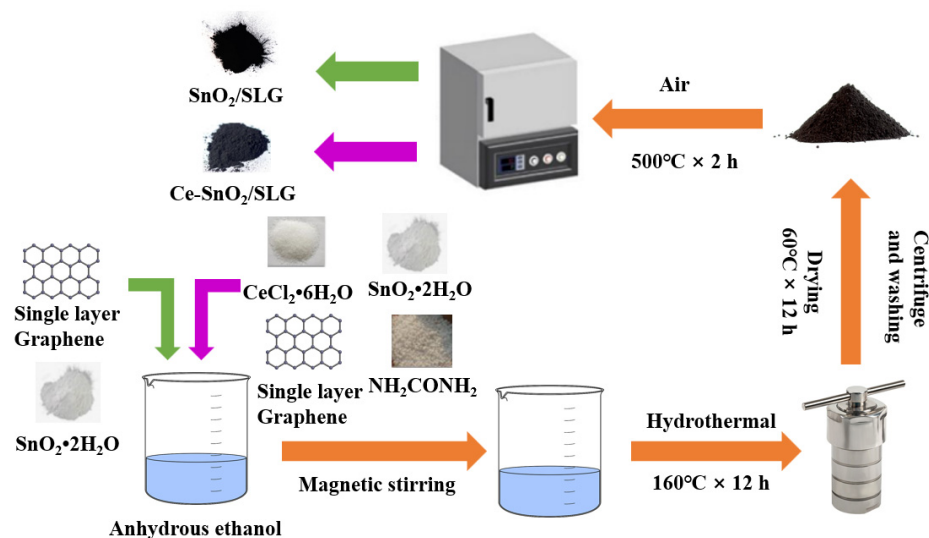


Figure 1. Synthetic scheme of the samples.

2.3. Characterization

The X-ray diffraction (XRD) pattern of the synthesized samples was obtained from the D/MAX-2200V (Riken Electric Co., Ltd., Tokyo, Japan) diffractometer system with $\text{Cu-K}\alpha$ radiation in the scanning range of $20\text{--}90$ degrees. Room-temperature Raman spectra of fabricated samples were acquired using a Microconfocal Raman spectrometer from 'InVia Qontor, Renishaw Ltd., Wotton-under-Edge, UK' with an excitation wavelength of 532 nm. The surface morphology and X-ray energy-dispersive spectroscopy (EDS) of the samples were recorded using a field emission scanning electron microscope (FESEM) from Japan Electronics JSM-IT800 (JEOL Ltd., Akishima, Japan). The transmission electron microscope (TEM) micrographs of samples have been obtained by means of 'JEM-F200' (JEOL Ltd., Akishima, Japan) operating at 200 keV. The X-ray photoelectron spectroscopy (XPS) spectrum of the sample was obtained from an X-ray photoelectron spectrometer manufactured by Thermo Fisher Scientific in the Loughborough, UK, using an $\text{Al-K}\alpha$ monochromatic X-ray spectrum.

2.4. Fabrication and Performance Test of the Gas Sensor

In this work, we utilized HHC1000 micro-hotplate gas-sensitive components provided by Micro & Nano Sensing Technologies Co., Ltd. (Hefei, China). As shown in Figure 2, these components are manufactured based on silicon microelectromechanical systems (MEMS) technology, specifically designed for the fabrication of metal oxide semiconductor (MOS) gas sensors. Featuring a suspended membrane structure, they are characterized by low power consumption and high reliability. The structure mainly includes interdigitated electrodes (IDE), an isolation membrane, a heater, and a support membrane. The IDE and sensing material form the sensing layer, which reacts with the target gas and converts changes in gas concentration into measurable electrical signals. The isolation membrane

prevents electrical connections between the heater and the IDE. The micro heater provides the necessary heating conditions for gas sensing, while the support membrane offers structural support to the sensitive area, ensuring the device's strength. The IDE leads are connected to a four-probe metal setup, which is encapsulated for sensing tests and data acquisition. The IDE is a flexible electrode with Pt.

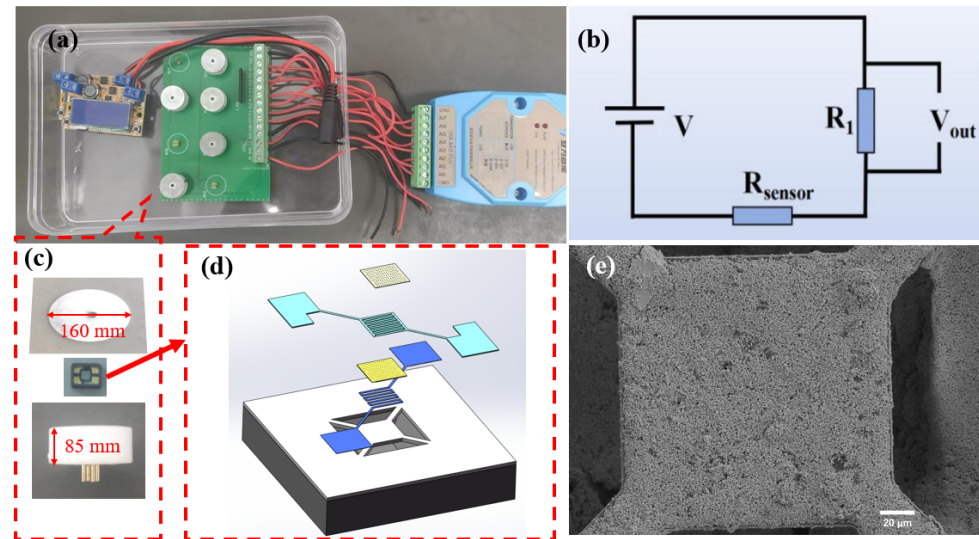


Figure 2. (a) Full device diagram of the gas sensitivity performance testing device; (b) circuit schematic diagram; (c) assembly diagram of the gas sensing element; (d) assembly diagram of gas-sensitive elements; (e) SEM image of the sensitive layer.

Before conducting gas sensing tests, the sensing material needs to be integrated into the micro-hotplate gas-sensitive component to form the sensor. The preparation process is as follows: a suitable amount of hydrogen-sensitive material and anhydrous ethanol are placed in an agate mortar and ground into a suspension. Using an ultra-fine paintbrush, a drop of the suspension is applied to the IDE area of the micro-hotplate gas-sensitive component to form a sensing film. After the suspension dries, the gas-sensitive component is heated and aged on a gas sensitivity test bench at 250 °C for one day to promote material deposition and performance stabilization, thereby ensuring reliable gas sensitivity data.

Gas sensitivity testing is performed on the intelligent analysis system of the Yawei Electronic Gas Sensitivity Tester, as depicted in Figure 2a. The measurement circuit for the gas sensor is illustrated in Figure 2b. The temperature (working temperature) of the heater at the chip's center is controlled by adjusting the heating voltage. The gas response is tested using a steady-state gas distribution method. During the testing process, a microinjector is used to introduce the required amount of target gas. In the circuit for measuring gas response, a load resistor (R_1) is connected in series with the MEMS gas sensor. The output voltage (V_{out}) is recorded 10 times per second. The relationship between the MEMS sensor's resistance (R) and V_{out} is shown in Equation (1):

$$R_{\text{sensor}} = (V - V_{\text{out}}) R_1 / V_{\text{out}} \quad (1)$$

This testing equipment features 8 channels for simultaneous testing of 8 sensor units. Each sensor unit comprises a base, a gas sensing element, and a bottom cover, as depicted in Figure 2c. The base transmits the electrical signals from the gas sensing element to the testing circuit board, enabling rapid collection of the changing signals. The gas-sensing element, pivotal to sensors, detects changes in hydrogen concentration in the external environment, resulting in resistance variations. The assembly diagram of gas sensing element is shown in Figure 2d. A magnetic attraction between the bottom cover and base stabilizes the gas sensing element, enhancing signal stability. When assessing the gas

sensing capabilities of these sensors, they are preheated to their operating temperature until their resistance stabilizes. Figure 2e presents a SEM image of the sensitive layer, measuring 150 μm in length and 150 μm in width.

The time taken by the sensor to achieve 90% of the total resistance change was defined as the response time in the case of adsorption or the recovery time in the case of desorption. The response of the sensor was measured between 190 and 350 $^{\circ}\text{C}$. The sensor response to the gas is defined as R_a/R_g . R_a is the resistance in the air, and R_g is the resistance in the target gas. Gas sensitivity tests were conducted under different concentrations of H_2 conditions. The entire experiment was conducted under a humidity of 20% and monitored using an analysis system. The carrier gas for the sensing measurements is air.

3. Results and Discussion

3.1. X-ray Diffraction

Figure 3 displays the XRD patterns of undoped and Ce-doped SLG/ SnO_2 nanoparticles. The sample's diffraction peaks align with the standard diffraction peaks of SnO_2 (PDF # 41-1445), suggesting that the concurrent doping with cerium does not harm or modify the crystal structure of SnO_2 . Moreover, the derived material possesses a pure cubic rutile structure. The crystallite size and lattice constant of all the samples were estimated by using Scherrer's formula:

$$D = 0.9\lambda / \beta \cos\theta \quad (2)$$

where λ is the wavelength of incident X-rays, θ is the Bragg's angle, β is the full width at a half maximum.

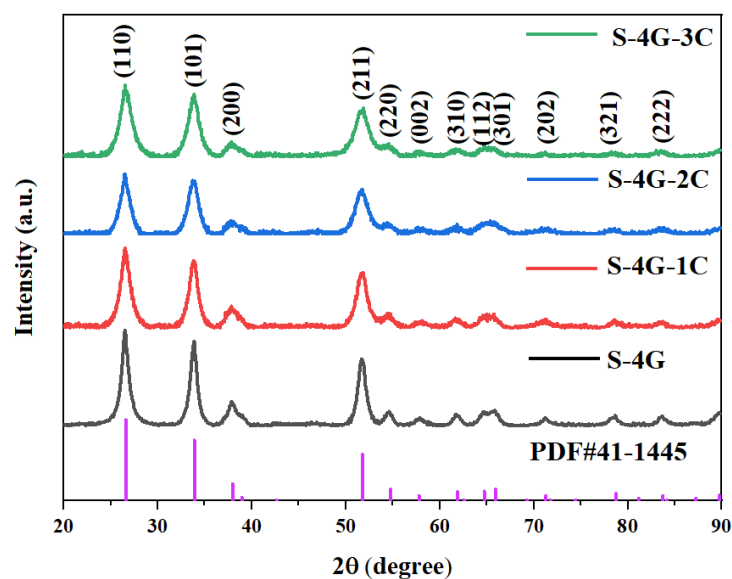


Figure 3. XRD patterns of undoped and Ce-doped SLG/ SnO_2 nanoparticles.

The calculated values of crystallite size of undoped and Ce-doped SLG/ SnO_2 nanoparticles are presented in Table 1. It is clear from tabulated values that crystallite size has reduced with an increase in Ce content which indicates that dopant suppressed the growth of SLG/ SnO_2 nanocrystallites. The smaller size can stimulate the quantum tunneling effect, which greatly promotes the gas-sensitive performance growth [35].

Table 1. Crystallite size of undoped and Ce-doped SLG/ SnO_2 nanoparticles.

Sample	S-4G	S-4G-1C	S-4G-2C	S-4G-3C
Ce content (mol%)	0	1	2	3
Crystallite size from XRD (nm)	9	8	5	6.1

3.2. Scanning Electron Microscopy

Figure 4a–d are SEM images of S-4G-2C and S-4G-3C materials, respectively. It can be seen that both S-4G-2C and S-4G-3C materials have nanosphere structures, and the diameter of the nanosphere structure in S-4G-2C is about 610 nm, while the diameter of the nanosphere structure in S-4G-3C is about 800 nm. At the same time, a certain degree of agglomeration phenomenon occurs, and the agglomeration phenomenon in S-4G-3C is relatively more severe. Therefore, S-4G-2C has a larger specific surface area compared to S-4G-3C. And from Figure 4b,d, it can be seen that the spherical surface of S-4G-2C is rougher, which can provide more active sites, facilitate the adsorption of more gases, and improve the gas sensing performance of the material. Therefore, an excessive addition of Ce leads to severe aggregation of Ce-SnO₂/SLG nanosphere materials, resulting in a decrease in specific surface area and active sites on the surface, thereby reducing the hydrogen sensitivity of the material [36,37].

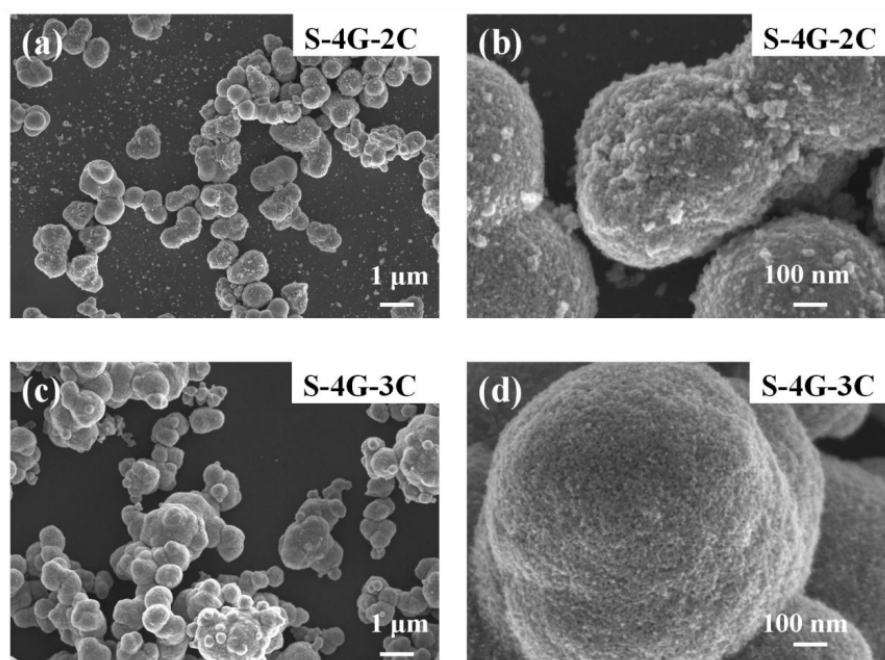


Figure 4. SEM image of (a) S-4G-2C; (b) S-4G-2C at a higher magnification; (c) S-4G-3C sample; (d) S-4G-3C at a higher magnification.

3.3. Transmission Electron Microscopy

The structural properties of synthesized nanoparticles were further studied using transmission electron microscopy. It can be seen that SnO₂ nanocrystallines were coated on the surface of the SLG material, with an average particle size of about 6.79 nm. The lattice stripe of SnO₂ NPs can be clearly seen from the Figure 5b HRTEM image, with a lattice spacing of 0.33 nm, corresponding to the rectangular rutile type (110) surface. As shown in Figure 5c, a series of diffraction rings belonging to SnO₂ can be seen in the selective electron diffraction pattern, which further shows that the prepared SnO₂ is of the rectangular rutile type and has a polycrystalline structure. The EDS image of S-4G-2C is shown in Figure 5d–h. It can be seen from the figure that Sn, O, C, and Ce elements are uniformly distributed on S-4G-2C, which also proves the successful preparation of the Ce-SnO₂/SLG material.

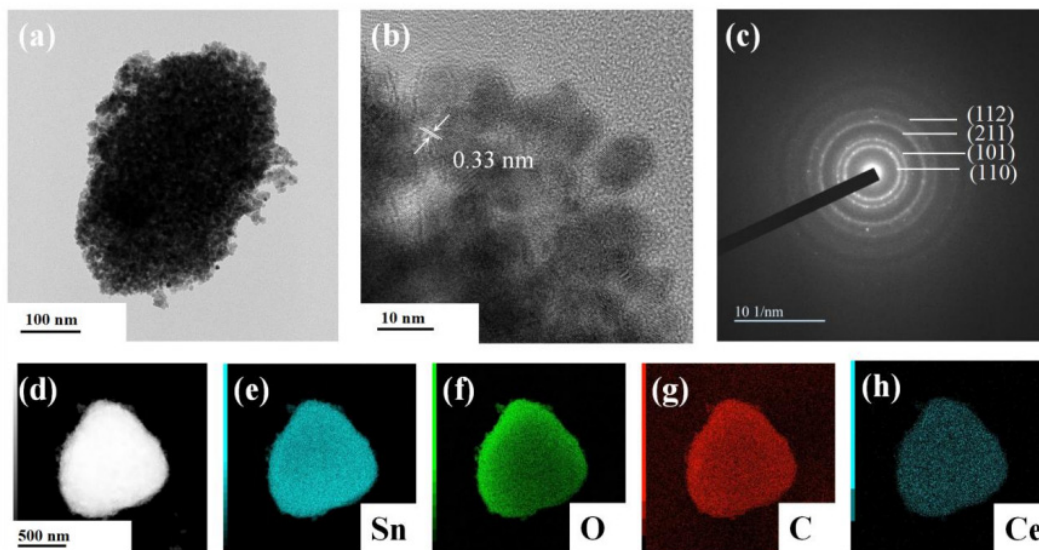


Figure 5. (a) TEM image; (b) HRTEM image; and (c) selected area electron diffraction image of S-4G-2C sample; (d–h) EDS spectra of the S-4G-2C sample: (d) selected region of the energy spectrum, (e) Sn element energy spectrum, (f) O element energy spectrum, (g) C element energy spectrum, and (h) Ce element energy spectrum.

3.4. X-ray Photoelectron Spectroscopy

Figure 6a shows the XPS full spectrum of S-4G-2C, where Sn 3d, C 1s, O 1s, and Ce 3d can be observed. Figure 6b shows the high-resolution XPS spectra of Sn 3d, where the Sn 3d_{5/2} peak appears at 486.7 eV and the Sn 3d_{3/2} peak is located at 495.1 eV, indicating that the chemical state of Sn is +4 valence. Figure 6c shows the high-resolution spectrum of C 1s in the S-4G-2C sample. It can be seen that it mainly has three characteristic peaks, located at 284.2 eV, 285.3 eV, and 288.6 eV, respectively, belonging to aromatic carbon (C-C), epoxy and alkoxy carbon (C-O), and hydroxyl carbon (C=O). The introduction of C=O and C-O indicates the formation of sp³ hybridization in the SLG structure, and the introduction of sp³ hybridization bonds will inevitably weaken sp² hybridization, and increase disorders and defects, which is conducive to increasing the surface-active sites of the material. As shown in Figure 6d, the high-resolution spectrum of O 1s can be divided into three peaks, corresponding to lattice oxygen (O_L), oxygen vacancies (O_V), and chemisorbed oxygen (O_C), respectively.

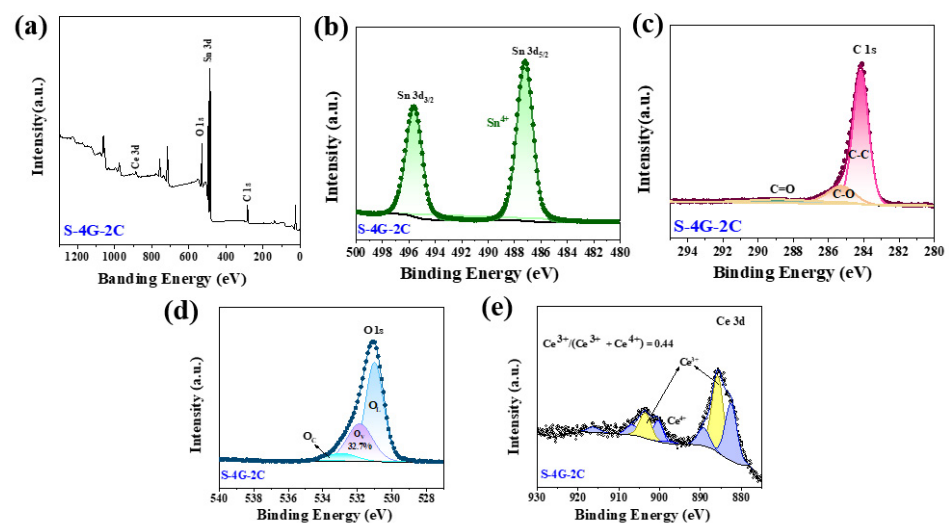


Figure 6. (a) XPS full spectrum of the S-4G-2C samples; high-resolution XPS spectra of (b) Sn 3d, (c) C 1s, (d) O 1s, and (e) Ce 3d.

Figure 7a shows the full spectrum of sample S-4G, indicating that the sample consists of Sn, O, and C elements. Figure 7b shows the high-resolution map of Sn 3d, in which the Sn 3d_{5/2} peak appears at 487.2 eV and the Sn 3d_{3/2} peak at 495.6 eV, indicating that the chemical state of Sn is +4 valence. Figure 7c shows the high-resolution map of C 1s in the S-4G sample. As can be seen from the figure, it mainly has three characteristic peaks at 284.6 eV, 285.6 eV, and 288.9 eV, belonging to the aromatic carbon (C-C), epoxy and alkoxy carbon (C-O), and hydroxyl carbon (C=O). The peak of C=O and C-O indicates that the sp³ hybrid is generated in the SLG structure [38]. The high-resolution map of Figure 7d can be divided into three peaks, corresponding to lattice oxygen (O_L, 529.0–529.5 eV), oxygen vacancy (O_V, 530.9–531.2 eV), and chemisorbed oxygen (O_C, 532.3–533.1 eV). Previous reports in the literature indicate that the surface oxygen state of most chemically resistive sensors has a great influence on their gas sensing performance.

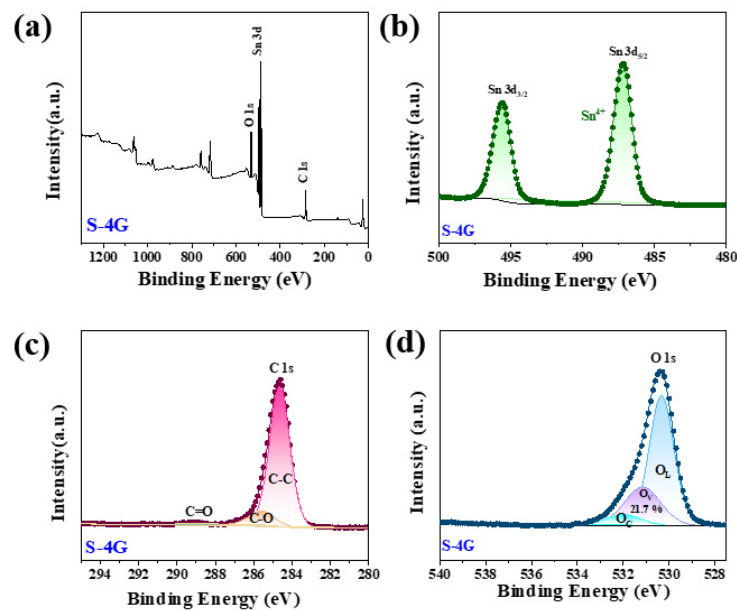


Figure 7. (a) XPS full spectrum of the S-4G samples; high-resolution XPS spectra of (b) Sn 3d; (c) C 1s; (d) O 1s.

The O_V ratio can effectively reflect the concentration of surface oxygen vacancies. It was found that the concentration of surface oxygen vacancies follows the order of S-4G-2C (32.7%) > S-4G (21.7%), and the response also follows the order of S-4G-2C (2.49) > S-4G (1.98), indicating that the concentration of oxygen vacancies greatly affects the response of the material. This is because abundant O_V generates a large number of free electrons to maintain high carrier mobility, which is conducive to improving the gas sensing performance of the material. The interaction between Ce and SLG is beneficial for increasing the oxygen vacancy content of the sample, thereby greatly improving the hydrogen sensing performance of the material.

3.5. Raman Spectroscopy

Raman spectroscopy is usually used to investigate the crystal defects, crystal structure, crystallinity, and size effects of oxide semiconductors. Figure 8 exhibits the Raman spectra of S-4G, S-4G-1C, S-4G-2C, and S-4G-3C samples. The D peak near 1350 cm⁻¹ represents the crystal defects of carbon atoms, and the G peak near 1580 cm⁻¹ represents the stretching vibration within the sp² hybridization plane of carbon atoms. I_(D)/I_(G) can reflect the degree of disorder in the sp² carbon domain within the graphene plane [39,40]. I_(D)/I_(G) can be used to evaluate defects in materials, and a larger I_(D)/I_(G) indicates more crystal defects in carbon materials. According to Raman calculations, S-4G-3C (I_(D)/I_(G) = 0.971) > S-4G-2C (I_(D)/I_(G) = 0.917) > S-4G-1C (I_(D)/I_(G) = 0.869) > S-4G (I_(D)/I_(G) = 0.349). As the Ce content

increases, the sample becomes more disordered and has more crystal structure defects, making the gas in the material easy to adsorb but difficult to desorb, resulting in a longer recovery time than the response time.

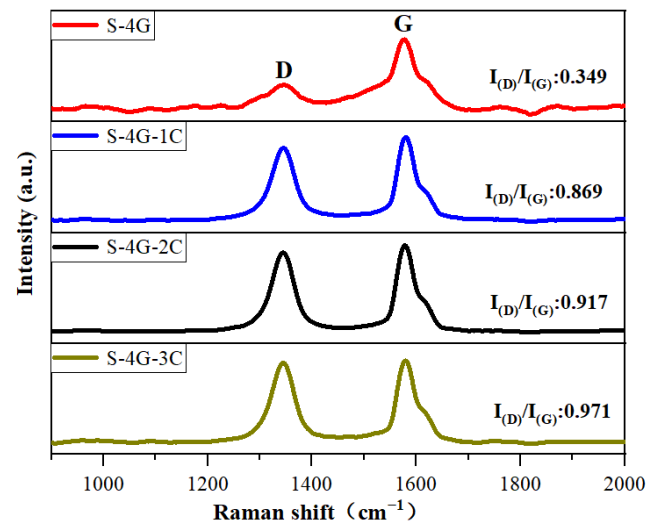


Figure 8. Raman spectra of the S-4G, S-4G-1C, S-4G-2C, and S-4G-3C samples.

3.6. Gas Sensing Properties

The optimal operating temperature and response is the major indicators for evaluating gas sensors, and their testing occupies the first priority in all gas sensitivity tests. Therefore, it is particularly important to determine the optimal operating temperature test, which plays a vital role in evaluating the performance of the gas sensor. In order to determine the optimal operating temperature of SnO₂, S-4G, S-4G-1C, S-4G-2C, and S-4G-3C from 190 °C to 345 °C, these samples were tested for different temperature responses of 10 ppm hydrogen (each set of experiments was repeated three times), as shown in Figure 9. The specific values are listed in Table 2. It can be seen that S-4G, S-4G-1C, S-4G-2C, and S-4G-3C all reach the maximum response at 250 °C, which are 1.98, 2.25, 2.49, and 1.61, respectively. The response of the dual-doped samples S-4G-1C and S-4G-2C at the optimal operating temperature increased by 13.6% and 25.75% compared to S-4G. And the S-4G-3C decreased by 18.69%.

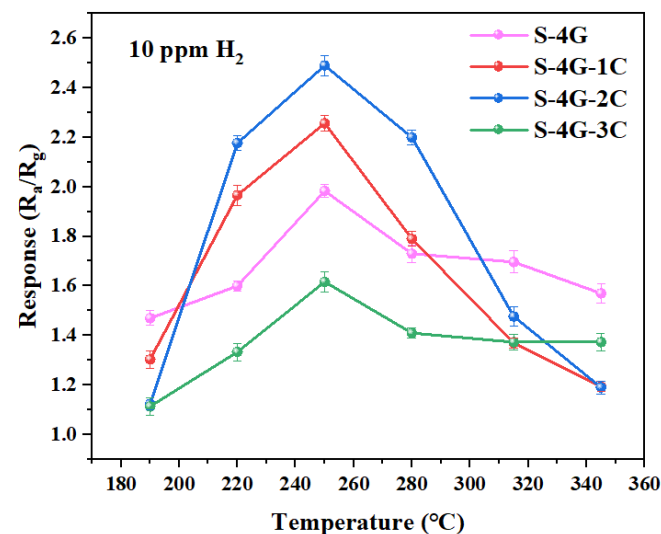


Figure 9. Response of the S-4G and S-4G-xC (x = 1, 2, 3) sensors to 10 ppm of H₂ at different temperatures.

Table 2. Response of the SnO₂, S-4G, and S-4G-xC (x = 1, 2, 3) sensors to 10 ppm of H₂ at different temperatures.

Sample	Response at Different Temperatures					
	190 °C	220 °C	250 °C	280 °C	315 °C	345 °C
S-4G	1.47	1.60	1.98	1.72	1.70	1.57
S-4G-1C	1.30	1.96	1.25	1.79	1.37	1.20
S-4G-2C	1.12	2.17	2.49	2.20	1.47	1.20
S-4G-3C	1.11	1.33	1.61	1.41	1.36	1.37

S-4G-2C reached the maximum response (2.49) of the whole system at 250 °C, namely, 2% Ce-SnO₂/SLG-4 mg was the optimal sample. It can be seen that the hydrogen-sensitive response of Ce-SnO₂/SLG was significantly higher than that of SnO₂/SLG sample. The higher response of doping is due to the good synergy among P-type semiconductor SLG material, N-type metal oxide semiconductor SnO₂, and N-type metal oxide semiconductor CeO₂. Compared with SnO₂/SLG, there are three heterojunction types: SLG, SnO₂, CeO₂, and the structural complexity of the material is significantly improved.

The response (t_{rs})/recovery (t_{rc}) time of S-4G and S-4G-xC (x = 1, 2, 3) at 250 °C was tested. As shown in Figure 10a–d, the response time of the doped sample (S-4G-1C 0.32 s; S-4G-2C: 0.46 s; S-4G-3C: 0.76 s) was significantly reduced from S-4G (1.02 s). The recovery time was significantly much greater than the response time. This may be related to the fact that graphene is prone to gas adsorption but difficult to desorb, and when gas molecules adsorb on the material surface, they usually release heat. When gas molecules desorb from the material surface, they need to absorb heat. The difference in energy changes during this adsorption and desorption process leads to a faster response speed of the material in gas detection applications, while the recovery speed may be relatively slow.

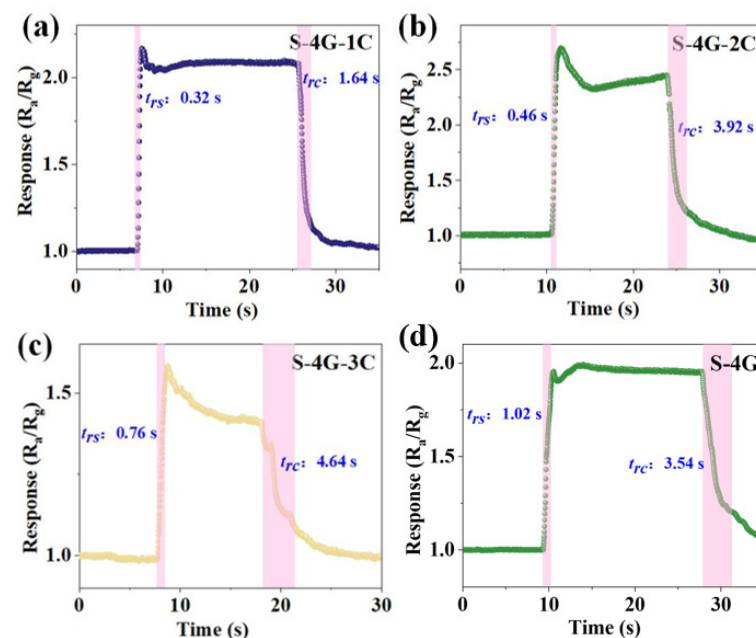
**Figure 10.** Response/recovery times for 10 ppm hydrogen at an operating temperature of 250 °C for (a) S-4G-1C; (b) S-4G-2C; (c) S-4G-3C; and (d) S-4G.

Figure 11a–d shows the response curves of the S-4G and S-4G-xC samples (x = 1, 2, 3) at 250 °C under different gas concentrations. The response of the test sample varied with the gas concentration, and the response always increased with the increase in gas concentration. The detection limit of the doped SLG/SnO₂ was 0.5 ppm. As shown in Figure 11e, the fitting curve of the sensor response is plotted with gas concentration as the horizontal

axis and response as the vertical axis, reflecting the linear relationship between response and hydrogen concentration. It can be seen that the S-4G-2C sample has a positive linear relationship, which allows for a better estimation of gas concentration in the environment based on the sensor response.

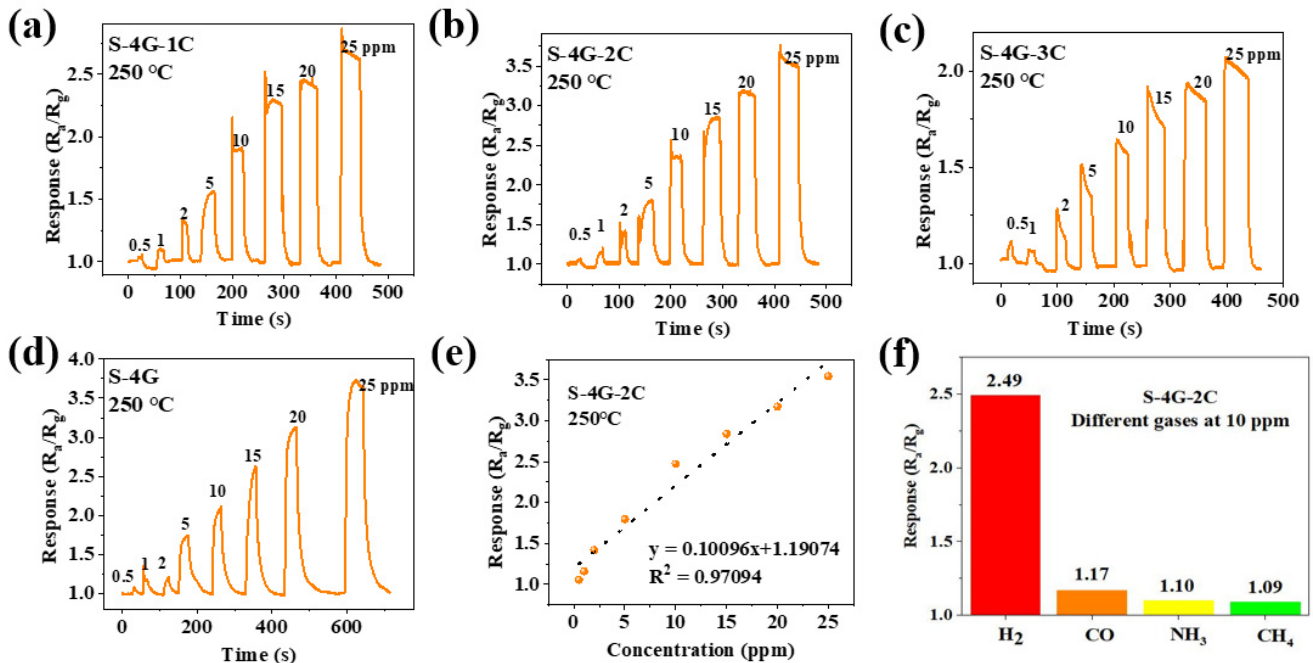


Figure 11. Response curves of (a) S-4G-1C; (b) S-4G-2C; (c) S-4G-3C; (d) S-4G at 250 °C under different H₂ concentrations. (e) Fitting curve of the response of S-4G-2C as a function of H₂ concentration. (f) Response of S-4G-2C to different gases (10 ppm) at 250 °C.

The selectivity of the sensor toward different interfering gases was tested. The response of the S-4G-2C sample to different gases such as hydrogen, carbon monoxide, ammonia, and methane at 10 ppm were tested at 250 °C. The results are shown in Figure 11f. The response of S-4G-2C samples to hydrogen was higher than those of the other gases. Ce-doped samples exhibited better selectivity toward hydrogen gas.

The two other important indicators for evaluating the performance of gas sensors are repeatability and stability. The dynamic response curve of the optimal doped sample S-4G-2C over four test cycles at a hydrogen concentration of 10 ppm at 250 °C is shown in Figure 12. From the figure, it can be seen that the gas sensing performance of the sample is relatively stable and the response did not significantly decreased, indicating that the sample has good stability and repeatability.

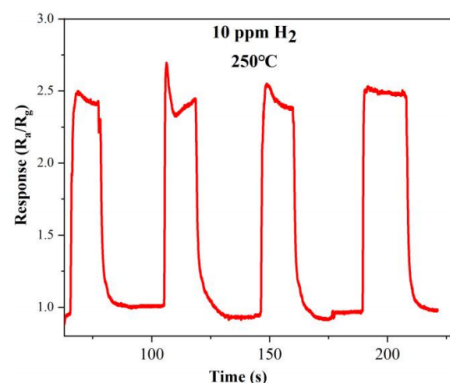


Figure 12. Repeatability of S-4G-2C in a 10 ppm hydrogen atmosphere at 250 °C.

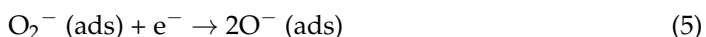
Additionally, the performance of the optimally doped sample S-4G-2C was compared to the other reported SnO₂-based sensors for hydrogen gas sensing (Table 3). It is evident that the sensor co-doped with rare earth Ce and single-layer graphene materials exhibits an extremely rapid response and recovery time, as well as a high response for hydrogen gas detection at relatively lower operating temperatures, confirming that Ce-SnO₂/SLG sensors have good application prospects and are suitable for hydrogen gas detection.

Table 3. Comparison between the present and previous studies on the H₂ gas response of different gas sensors.

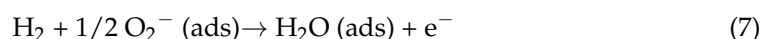
Material	Working Temperature (°C)	Concentration (ppm)	Response	Response Time (s)	Recovery Time (s)	Ref.
Au-functionalized ZnO-branched SnO ₂ NWs	300	10	13.07	190	351	[41]
SnO ₂ thin film with a Pd island	300	250	28	3	50	[42]
Graphene-loaded Al-SnO ₂ nanotubes	300	100	23.8	2.2	1.4	[24]
S-4G-2C	250	10	2.49	0.46	3.92	This work

3.7. Sensing Mechanism

It is generally accepted that the sensing response arises from changes in the resistance of gas sensors, induced by the adsorption and desorption of gas molecules on the material surface. The detailed sensing mechanism has been described in references [43,44]. The oxygen vacancies play a critical role in the sensing performance. At different temperatures, oxygen molecules will chemically adsorb on the surface of SnO₂ in the form of O₂[−], O[−], and O^{2−}:



Moreover, the oxygen species that have been adsorbed can react with H₂ molecules on the surface, following the equation provided below:



The interaction between the reducing gas and oxygen results in a reduction in adsorbed oxygen, which in turn reverses the band bending and enhances conductivity. SnO₂ is an N-type semiconductor, thereby its conductivity is primarily influenced by the quantity of oxygen adsorbed on its surface. Oxygen ions are formed as oxygen absorbs electrons from the conduction band of tin oxide, leading to the creation of vacancies and subsequently high resistance. When SnO₂ nanoparticles are exposed to H₂, the chemisorbed oxygen anions on the surface of tin oxide react with hydrogen, leading to the removal of chemisorbed oxygen anions and the oxidation of H₂ molecules. Consequently, the free electrons captured by these oxygen molecules are released back to the conduction band of tin oxide, resulting in a decrease in resistance.

The presence of both Ce³⁺ and Ce⁴⁺ on the surface of Ce-doped SnO₂ hydrogen-sensitive materials generates a significant number of additional oxygen vacancies. Ce⁴⁺, being an oxidizing ion, readily captures electrons, resulting in the formation of Ce³⁺ ions and the concomitant creation of numerous oxygen vacancies [45]. Moreover, at the interface of Ce-SnO₂/SLG composites, multiple heterogeneous interfaces exist. Specifically, an n-n

junction forms between CeO₂ and SnO₂, and a p–n junction between SnO₂ and SLG [46]. Because CeO₂ has a lower work function than SnO₂, the n–n heterojunction facilitates a greater transfer of electrons from CeO₂ to SnO₂. This leads to more holes on SLG moving to SnO₂, and vice versa, until a dynamic equilibrium is reached. This facilitation thickens the depletion layers between CeO₂ and SnO₂, as well as between SnO₂ and SLG, thereby increasing the material's resistance in air. In a hydrogen environment, hydrogen molecules react with adsorbed oxygen on the material surface, releasing electrons back into SnO₂. This reaction diminishes the depletion layer's depth, reduces the energy band's curvature, and lowers the potential barrier. Consequently, charge carriers transfer more readily, enhancing the material's conductivity and significantly reducing its resistance.

4. Conclusions

In this work, Ce-SnO₂/SLG composite materials were prepared using a hydrothermal method, which has the advantages of simple operation, low cost, and the ability to achieve large-scale production. Among them, the 2% Ce-SnO₂/SLG-4 mg composite material has the best hydrogen sensitivity performance at a humidity of 20%, with a high response rate of 2.49. The reaction time decreased from 1.02 s to 0.46 s, indicating an extremely low response time. When detecting 10 ppm H₂ at 250 °C, the response and recovery times are 0.46 s and 3.92 s, respectively. Additionally, the sensor exhibits excellent selectivity and reproducibility for hydrogen gas. The reason why doping Ce enhances the hydrogen sensitivity of SnO₂ can be attributed to the following: an increase in Ce doping leads to increased disorder and more defects in the crystal structure of SLG, favoring the creation of more active sites; and Ce doping inhibits the growth of SnO₂ nanocrystals. Moreover, Ce doping enhances the concentration of oxygen vacancies (32.7%), thereby increasing active sites and boosting the material's hydrogen sensitivity. Moreover, Ce doping facilitates the formation of n–n and p–n heterojunctions, which, through their combined effect, enhance charge carrier transfer, increase the material's depletion layer thickness, and elevate its hydrogen sensitivity.

Author Contributions: Conceptualization, Z.J. and L.W.; Investigation, X.X., J.X., S.H. and T.L.; Project administration, J.X., S.H. and T.L.; Resources, J.X., S.H. and T.L.; Supervision, X.H.; Writing—original draft, Z.J.; Writing—review and editing, X.X., S.H., T.L. and X.H. All authors have read and agreed to the published version of the manuscript.

Funding: This research was funded by the National Natural Science Foundation of China (grants no. 12373078), and the Foundation Strengthening Program in the Technical Field of China (grants no. 2020-JCJQ-JJ-418).

Institutional Review Board Statement: Not applicable.

Informed Consent Statement: Not applicable.

Data Availability Statement: The original contributions presented in the study are included in the article, further inquiries can be directed to the corresponding author.

Conflicts of Interest: Authors Jie Xiang, Shuiming Huang, Tao Lu were employed by the company Shanghai King Material Technology Ltd. The remaining authors declare that the research was conducted in the absence of any commercial or financial relationships that could be construed as a potential conflict of interest.

References

1. Wang, J.; Kwak, Y.; Lee, I.-y.; Maeng, S.; Kim, G.-H. Highly responsive hydrogen gas sensing by partially reduced graphite oxide thin films at room temperature. *Carbon* **2012**, *50*, 4061–4067. [[CrossRef](#)]
2. Gao, L.; Tian, Y.; Hussain, A.; Guan, Y.; Xu, G. Recent developments and challenges in resistance-based hydrogen gas sensors based on metal oxide semiconductors. *Anal. Bioanal. Chem.* **2024**, *416*, 3697–3715. [[CrossRef](#)]
3. Liu, P.; Han, X. Comparative analysis on similarities and differences of hydrogen energy development in the World's top 4 largest economies: A novel framework. *Int. J. Hydrogen Energy* **2022**, *47*, 9485–9503.
4. Anand, K.; Singh, O.; Singh, M.P.; Kaur, J.; Singh, R.C. Hydrogen sensor based on graphene/ZnO nanocomposite. *Sens. Actuators B-Chem.* **2014**, *195*, 409–415. [[CrossRef](#)]

5. Wang, J.; Singh, B.; Park, J.-H.; Rathi, S.; Lee, I.-y.; Maeng, S.; Joh, H.-I.; Lee, C.-H.; Kim, G.-H. Dielectrophoresis of graphene oxide nanostructures for hydrogen gas sensor at room temperature. *Sens. Actuators B-Chem.* **2014**, *194*, 296–302. [[CrossRef](#)]
6. Chauhan, P.S.; Bhattacharya, S. Hydrogen gas sensing methods, materials, and approach to achieve parts per billion level detection: A review. *Int. J. Hydrogen Energy* **2019**, *44*, 26076–26099. [[CrossRef](#)]
7. Abdulhameed, A.; Mahnashi, Y. Fabrication of carbon nanotube/titanium dioxide nanomaterials-based hydrogen sensor using novel two-stage dielectrophoresis process. *Mater. Sci. Semicond. Process.* **2023**, *167*, 107794–107805. [[CrossRef](#)]
8. Singh, G.; Kohli, N.; Singh, R.C. Preparation and characterization of Eu-doped SnO₂ nanostructures for hydrogen gas sensing. *J. Mater. Sci.-Mater. Electron.* **2017**, *28*, 2257–2266. [[CrossRef](#)]
9. Enachi, M.; Lupan, O.; Braniste, T.; Sarua, A.; Chow, L.; Mishra, Y.K.; Gedamu, D.; Adelung, R.; Tiginyanu, I. Integration of individual TiO₂ nanotube on the chip: Nanodevice for hydrogen sensing. *Phys. Status Solidi-Rapid Res. Lett.* **2015**, *9*, 171–174. [[CrossRef](#)]
10. Singh, O.; Singh, R.C. Enhancement in ethanol sensing response by surface activation of ZnO with SnO₂. *Mater. Res. Bull.* **2012**, *47*, 557–561. [[CrossRef](#)]
11. Cretu, V.; Postica, V.; Mishra, A.K.; Hoppe, M.; Tiginyanu, I.; Mishra, Y.K.; Chow, L.; de Leeuw, N.H.; Adelung, R.; Lupan, O. Synthesis, characterization and DFT studies of zinc-doped copper oxide nanocrystals for gas sensing applications. *J. Mater. Chem. A* **2016**, *4*, 6527–6539. [[CrossRef](#)]
12. Kohli, N.; Singh, O.; Singh, R.C. Influence of pH on particle size and sensing response of chemically synthesized chromium oxide nanoparticles to alcohols. *Sens. Actuators B-Chem.* **2011**, *158*, 259–264. [[CrossRef](#)]
13. Ab Kadir, R.; Li, Z.; Sadek, A.Z.; Rani, R.A.; Zoolfakar, A.S.; Field, M.R.; Ou, J.Z.; Chrimes, A.F.; Kalantar-zadeh, K. Electrospun Granular Hollow SnO₂ Nanofibers Hydrogen Gas Sensors Operating at Low Temperatures. *J. Phys. Chem. C* **2014**, *118*, 3129–3139. [[CrossRef](#)]
14. Wang, Y.; Liu, C.; Wang, L.; Liu, J.; Zhang, B.; Gao, Y.; Sun, P.; Sun, Y.; Zhang, T.; Lu, G. Horseshoe-shaped SnO₂ with annulus-like mesoporous for ethanol gas sensing application. *Sens. Actuators B-Chem.* **2017**, *240*, 1321–1329. [[CrossRef](#)]
15. Kida, T.; Fujiyama, S.; Suematsu, K.; Yuasa, M.; Shimano, K. Pore and Particle Size Control of Gas Sensing Films Using SnO₂ Nanoparticles Synthesized by Seed-Mediated Growth: Design of Highly Sensitive Gas Sensors. *J. Phys. Chem. C* **2013**, *117*, 17574–17582. [[CrossRef](#)]
16. Lupan, O.; Postica, V.; Labat, F.; Ciofini, I.; Pauporte, T.; Adelung, R. Ultra-sensitive and selective hydrogen nanosensor with fast response at room temperature based on a single Pd/ZnO nanowire. *Sens. Actuators B-Chem.* **2018**, *254*, 1259–1270. [[CrossRef](#)]
17. Cho, N.G.; Whitfield, G.C.; Yang, D.J.; Kim, H.-G.; Tuller, H.L.; Kim, I.-D. Facile Synthesis of Pt-Functionalized SnO₂ Hollow Hemispheres and Their Gas Sensing Properties. *J. Electrochem. Soc.* **2010**, *157*, J435–J439. [[CrossRef](#)]
18. Lin, Z.; Li, N.; Chen, Z.; Fu, P. The effect of Ni doping concentration on the gas sensing properties of Ni doped SnO₂. *Sens. Actuators B-Chem.* **2017**, *239*, 501–510. [[CrossRef](#)]
19. Lin, Y.; Wei, W.; Li, Y.; Li, F.; Zhou, J.; Sun, D.; Chen, Y.; Ruan, S. Preparation of Pd nanoparticle-decorated hollow SnO₂ nanofibers and their enhanced formaldehyde sensing properties. *J. Alloys Compd.* **2015**, *651*, 690–698. [[CrossRef](#)]
20. Shaalan, N.M.; Yamazaki, T.; Kikuta, T. Influence of morphology and structure geometry on NO₂ gas-sensing characteristics of SnO₂ nanostructures synthesized via a thermal evaporation method. *Sens. Actuators B-Chem.* **2011**, *153*, 11–16. [[CrossRef](#)]
21. Chen, Y.; Yu, L.; Feng, D.; Zhuo, M.; Zhang, M.; Zhang, E.; Xu, Z.; Li, Q.; Wang, T. Superior ethanol-sensing properties based on Ni-doped SnO₂ p-n heterojunction hollow spheres. *Sens. Actuators B-Chem.* **2012**, *166*, 61–67. [[CrossRef](#)]
22. Xiao, L.; Shu, S.; Liu, S. A facile synthesis of Pd-doped SnO₂ hollow microcubes with enhanced sensing performance. *Sens. Actuators B-Chem.* **2015**, *221*, 120–126. [[CrossRef](#)]
23. Meyer, J.C.; Girit, C.O.; Crommie, M.F.; Zettl, A. Imaging and dynamics of light atoms and molecules on graphene. *Nature* **2008**, *454*, 319–322. [[CrossRef](#)] [[PubMed](#)]
24. Reddy, C.S.; Zhang, L.; Qiu, Y.; Chen, Y.; Reddy, A.S.; Reddy, P.S.; Dugasani, S.R. Investigation of hydrogen sensing properties of graphene/Al-SnO₂ composite nanotubes derived from electrospinning. *J. Ind. Eng. Chem.* **2018**, *63*, 411–419.
25. Li, G.; Shen, Y.; Zhao, S.; Li, A.; Han, C.; Zhao, Q.; Wei, D.; Yuan, Z.; Meng, F. Novel sensitizer AuxSn modify rGO-SnO₂ nanocomposites for enhancing detection of sub-ppm H₂. *Sens. Actuators B-Chem.* **2022**, *373*, 132656. [[CrossRef](#)]
26. Kim, H.; Pak, Y.; Jeong, Y.; Kim, W.; Kim, J.; Jung, G.Y. Amorphous Pd-assisted H₂ detection of ZnO nanorod gas sensor with enhanced sensitivity and stability. *Sens. Actuators B-Chem.* **2018**, *262*, 460–468. [[CrossRef](#)]
27. Lupan, O.; Postica, V.; Wolff, N.; Su, J.; Labat, F.; Ciofini, I.; Cavers, H.; Adelung, R.; Polonskyi, O.; Faupel, F.; et al. Low-Temperature Solution Synthesis of Au-Modified ZnO Nanowires for Highly Efficient Hydrogen Nanosensors. *ACS Appl. Mater. Interfaces* **2019**, *11*, 32115–32126. [[CrossRef](#)]
28. Li, T.; Zhou, P.; Zhao, S.; Han, C.; Wei, D.; Shen, Y.; Liu, T. NH₃ sensing performance of Pt-doped WO₃•0.33H₂O microshuttles induced from scheelite leaching solution. *Vacuum* **2021**, *184*, 109936. [[CrossRef](#)]
29. Liu, B.; Cai, D.; Liu, Y.; Wang, D.; Wang, L.; Wang, Y.; Li, H.; Li, Q.; Wang, T. Improved room-temperature hydrogen sensing performance of directly formed Pd/WO₃ nanocomposite. *Sens. Actuators B-Chem.* **2014**, *193*, 28–34. [[CrossRef](#)]
30. Kumar, S.; Lawaniya, S.D.; Agarwal, S.; Yu, Y.-T.; Nelamarri, S.R.; Kumar, M.; Mishra, Y.K.; Awasthi, K. Optimization of Pt nanoparticles loading in ZnO for highly selective and stable hydrogen gas sensor at reduced working temperature. *Sens. Actuators B-Chem.* **2023**, *375*, 132943. [[CrossRef](#)]

31. Boudjahem, A.-G.; Bettahar, M.M. Effect of oxidative pre-treatment on hydrogen spillover for a Ni/SiO₂ catalyst. *J. Mol. Catal. A-Chem.* **2017**, *426*, 190–197. [[CrossRef](#)]
32. Singh, G.; Virpal; Singh, R.C. Highly sensitive gas sensor based on Er-doped SnO₂ nanostructures and its temperature dependent selectivity towards hydrogen and ethanol. *Sens. Actuators B-Chem.* **2019**, *282*, 373–383. [[CrossRef](#)]
33. Motaung, D.E.; Mhlongo, G.H.; Makgwane, P.R.; Dhonge, B.P.; Cummings, F.R.; Swart, H.C.; Ray, S.S. Ultra-high sensitive and selective H₂ gas sensor manifested by interface of n-n heterostructure of CeO₂-SnO₂ nanoparticles. *Sens. Actuators B-Chem.* **2018**, *254*, 984–995. [[CrossRef](#)]
34. Fang, J.Y. Study on the Effects of Ce and Single Layer Graphene Doping on the Sensing Performance and Mechanism of SnO₂ Hydrogen Sensitive Materials. Master's Thesis, Shanghai University, Shanghai, China, 2024.
35. Sui, L.-L.; Xu, Y.-M.; Zhang, X.-F.; Cheng, X.-L.; Gao, S.; Zhao, H.; Cai, Z.; Huo, L.-H. Construction of three-dimensional flower-like α -MoO₃ with hierarchical structure for highly selective triethylamine sensor. *Sens. Actuators B-Chem.* **2015**, *208*, 406–414. [[CrossRef](#)]
36. Chen, L.; Shi, H.; Ye, C.; Xia, X.; Li, Y.; Pan, C.; Song, Y.; Liu, J.; Dong, H.; Wang, D.; et al. Enhanced ethanol-sensing characteristics of Au decorated In-doped SnO₂ porous nanotubes at low working temperature. *Sens. Actuators B-Chem.* **2023**, *375*, 132864. [[CrossRef](#)]
37. Li, Z.; Yang, Q.; Wu, Y.; He, Y.; Chen, J.; Wang, J. La³⁺ doped SnO₂ nanofibers for rapid and selective H₂ sensor with long range linearity. *Int. J. Hydrogen Energy* **2019**, *44*, 8659–8668. [[CrossRef](#)]
38. Hu, J.; Chen, M.; Rong, Q.; Zhang, Y.; Wang, H.; Zhang, D.; Zhao, X.; Zhou, S.; Zi, B.; Zhao, J.; et al. Formaldehyde sensing performance of reduced graphene oxide-wrapped hollow SnO₂ nanospheres composites. *Sens. Actuators B-Chem.* **2020**, *375*, 132864. [[CrossRef](#)]
39. Si, R.; Xu, Y.; Shen, C.; Jiang, H.; Lei, M.; Guo, X.; Xie, S.; Gao, S.; Zhang, S. High-Selectivity Laminated Gas Sensor Based on Characteristic Peak under Temperature Modulation. *ACS Sens.* **2024**, *9*, 674–688. [[CrossRef](#)]
40. Inyawilert, K.; Wisitsoraat, A.; Sriprachauwong, C.; Tuantranont, A.; Phanichphant, S.; Liewhiran, C. Rapid ethanol sensor based on electrolytically-exfoliated graphene-loaded flame-made In-doped SnO₂ composite film. *Sens. Actuators B-Chem.* **2015**, *209*, 40–55. [[CrossRef](#)]
41. Choi, M.S.; Bang, J.H.; Mirzaei, A.; Oum, W.; Na, H.G.; Jin, C.; Kim, S.S.; Kim, H.W. Promotional effects of ZnO-branching and Au-functionalization on the surface of SnO₂ nanowires for NO₂ sensing. *J. Alloys Compd.* **2019**, *786*, 27–39. [[CrossRef](#)]
42. Nguyen Van, T.; Nguyen Viet, C.; Nguyen Van, D.; Hoang Si, H.; Nguyen, H.; Nguyen Duc, H.; Nguyen Van, H. Fabrication of highly sensitive and selective H₂ gas sensor based on SnO₂ thin film sensitized with micro-sized Pd islands. *J. Hazard. Mater.* **2016**, *301*, 433–442. [[PubMed](#)]
43. Zhao, Q.; Deng, X.; Ding, M.; Gan, L.; Zhai, T.; Xu, X. One-pot synthesis of Zn-doped SnO₂ nanosheet-based hierarchical architectures as a glycol gas sensor and photocatalyst. *CrystEngComm* **2015**, *17*, 4394–4401. [[CrossRef](#)]
44. Gyger, F.; Hübner, M.; Feldmann, C.; Barsan, N.; Weimar, U. Nanoscale SnO₂ Hollow Spheres and Their Application as a Gas-Sensing Material. *Chem. Mater.* **2010**, *22*, 4821–4827. [[CrossRef](#)]
45. Nadargi, D.Y.; Umar, A.; Nadargi, J.D.; Lokare, S.A.; Akbar, S.; Mulla, I.S.; Suryavanshi, S.S.; Bhandari, N.L.; Chaskar, M.G. Gas sensors and factors influencing sensing mechanism with a special focus on MOS sensors. *J. Mater. Sci.* **2023**, *58*, 559–582. [[CrossRef](#)]
46. Ahemad, M.J.; Hyung, S.-K.; Yun, H.; Im, M.; Lee, E.; Choi, J.H.; Kim, T.-W.; Lee, S.-K.; Moon, B.J.; Bae, S. In-situ Synthesis of Pd/WO₃ Nanocomposites for Low-Temperature Hydrogen Gas Sensing. *Appl. Sci. Conver. Technol.* **2023**, *32*, 100–103. [[CrossRef](#)]

Disclaimer/Publisher's Note: The statements, opinions and data contained in all publications are solely those of the individual author(s) and contributor(s) and not of MDPI and/or the editor(s). MDPI and/or the editor(s) disclaim responsibility for any injury to people or property resulting from any ideas, methods, instructions or products referred to in the content.